PERIDYNAMIC BEAMS, PLATES, AND SHELLS:

A NONORDINARY, STATE-BASED MODEL

APPROVED BY SUPERVISING COMMITTEE:

_____

John T. Foster, Ph.D., Chair

_____

Yusheng Feng, Ph.D.

_____

Walter Richardson, Ph.D.

_____

James Walker, Ph.D.

_____

Xiaowei Zeng, Ph.D.

Accepted: _____

Dean, Graduate School

DEDICATION

I would like to dedicate this dissertation to the memory of Thomas John O'Grady II, a passionate father and a passionate engineer

PERIDYNAMIC BEAMS, PLATES, AND SHELLS:

A NONORDINARY, STATE-BASED MODEL

by

JAMES O'GRADY, M.S.M.E.

DISSERTATION
Presented to the Graduate Faculty of
The University of Texas at San Antonio
In Partial Fulfillment
Of the Requirements
For the Degree of

DOCTOR OF PHILOSOPHY IN MECHANICAL ENGINEERING

THE UNIVERSITY OF TEXAS AT SAN ANTONIO
College of Engineering
Department of Mechanical Engineering
September 2014

ACKNOWLEDGEMENTS

I would like to thank my advisor, Dr. John Foster, for steering me onto a road I never knew existed and for pointing me at such an excellent problem.

Most of all, I would like to thank my wife, who has been endlessly supportive.

This Masters Thesis/Recital Document or Doctoral Dissertation was produced in accordance with guidelines which permit the inclusion as part of the Masters Thesis/Recital Document or Doctoral Dissertation the text of an original paper, or papers, submitted for publication. The Masters Thesis/Recital Document or Doctoral Dissertation must still conform to all other requirements explained in the Guide for the Preparation of a Masters Thesis/Recital Document or Doctoral Dissertation at The University of Texas at San Antonio. It must include a comprehensive abstract, a full introduction and literature review, and a final overall conclusion. Additional material (procedural and design data as well as descriptions of equipment) must be provided in sufficient detail to allow a clear and precise judgment to be made of the importance and originality of the research reported.

It is acceptable for this Masters Thesis/Recital Document or Doctoral Dissertation to include as chapters authentic copies of papers already published, provided these meet type size, margin, and legibility requirements. In such cases, connecting texts, which provide logical bridges between different manuscripts, are mandatory. Where the student is not the sole author of a manuscript, the student is required to make an explicit statement in the introductory material to that manuscript describing the students contribution to the work and acknowledging the contribution of the other author(s). The signatures of the Supervising Committee which precede all other material in the Masters Thesis/Recital Document or Doctoral Dissertation attest to the accuracy of this statement.

September 2014

PERIDYNAMIC BEAMS, PLATES, AND SHELLS:

A NONORDINARY, STATE-BASED MODEL

James O'Grady, Ph.D.
The University of Texas at San Antonio, 2014

Supervising Professor: John T. Foster, Ph.D., Chair

Peridynamics is a nonlocal formulation of continuum mechanics in which forces are calculated as integral functions of displacement fields rather than spatial derivatives. The peridynamic model has major advantages over classical continuum mechanics when displacements are discontinuous, such as in the case of material failure. While multiple peridynamic material models capture the behavior of solid materials, not all structures are conveniently analyzed as solids. Finite Element Analysis often uses 1D and 2D elements to model thin features that would otherwise require a great number of 3D elements, but peridynamic thin features remain underdeveloped despite great interest in the engineering community. This work develops nonordinary state-based peridynamic models for the simulation of thin features. Beginning from an example nonordinary state-based model, lower dimensional peridynamic models of plates, beams, and shells are developed and validated against classical models. These peridynamic models are extended to incorporate brittle and plastic material failure, compounding the peridynamic advantages of discontinuity handling with the computational simplicity of reduced-dimension features. Once validated, these models will allow peridynamic modeling of complex structures such as aircraft skin that may experience damage from internal forces or external impacts.

TABLE OF CONTENTS

LIST OF TABLES

LIST OF FIGURES

Chapter 4: MODEL DEVELOPMENT

4.1   Bond Pair Material Model

Consider the material model illustrated in fig. 4.1 in which every bond-vector originating from a point is connected by a rotational spring to its opposite originating from that same point. If we call
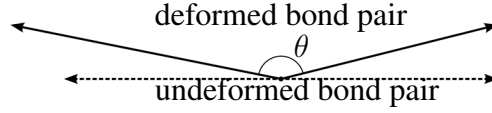
Figure 4.1: Illustration of a bond pair model that resists angular deformation

the deformed angle between these bonds θ, and choose the potential energy of that spring to be $w(\boldsymbol{\xi}) = \omega(\boldsymbol{\xi})\alpha[1 + \cos(\theta)]$ for the bond pair $\boldsymbol{\xi}$ and $-\boldsymbol{\xi}$, we can recover the non-ordinary force state proposed by Silling in [64] by taking the Fréchet derivative. For the derivation and a description of the Fréchet derivative see appendix A.

$$\underline{\mathbf{T}}\langle\boldsymbol{\xi}\rangle = \nabla w(\underline{\mathbf{Y}}\langle\boldsymbol{\xi}\rangle)$$

$$= \omega(\boldsymbol{\xi})\frac{-\alpha}{|\underline{\mathbf{Y}}\langle\boldsymbol{\xi}\rangle|}\frac{\underline{\mathbf{Y}}\langle\boldsymbol{\xi}\rangle}{|\underline{\mathbf{Y}}\langle\boldsymbol{\xi}\rangle|} \times \left[\frac{\underline{\mathbf{Y}}\langle\boldsymbol{\xi}\rangle}{|\underline{\mathbf{Y}}\langle\boldsymbol{\xi}\rangle|} \times \frac{\underline{\mathbf{Y}}\langle-\boldsymbol{\xi}\rangle}{|\underline{\mathbf{Y}}\langle-\boldsymbol{\xi}\rangle|}\right] \tag{4.1}$$

Though it looks complex, eq. (4.1) indicates a bond force perpendicular to the deformed bond and in the plane containing both the deformed bond and its partner as illustrated in fig. 4.2. The force magnitude is proportional to the sine of the angle between the bonds divided by the length of the deformed bond. This response is consistent with the idea of a rotational spring between bonds as
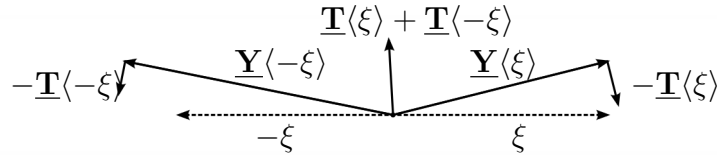
Figure 4.2: Deformation and force vector states

long as the change in angle is small. Because the potential energy and force states are functions

of *pairs* of peridynamic bonds, we will call this formulation a *bond-pair model*. Other choices for the bond-pair potential function, such as $w = (\pi - \theta)^2$, are also possible, but result in more mathematically complex analysis.

4.2 Bond Pair Beam in Bending

The simplest application of our bond-pair based peridynamic model is that of fig. 4.3, a beam in transverse bending. Much of the material in this section can also be found in [54].
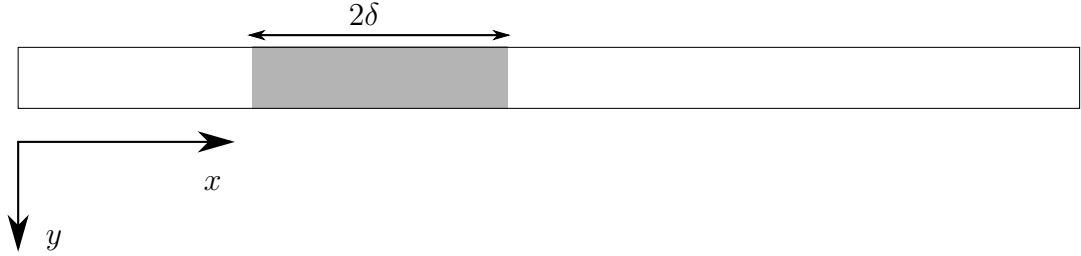
Figure 4.3: A continuous peridynamic beam with horizon δ

4.2.1 Energy Equivalence

To determine an appropriate choice of α for eq. (4.1), we desire our peridynamic model to have an equivalent strain energy density to a classical Euler-Bernoulli beam in the *local limit*, i.e. when the nonlocal length scale vanishes. We will begin with the assumptions from Euler beam theory: the length of the beam is much greater than thickness, vertical displacements are small, and rotations are small. For small vertical displacements (i.e. $\sin\theta \approx \theta$) we have

$$\theta(\underline{\mathbf{Y}}\langle\xi\rangle, \underline{\mathbf{Y}}\langle-\xi\rangle) \approx \pi - \frac{v(x+\xi) - 2v(x) + v(x-\xi)}{\xi}, \tag{4.2}$$

where v is the vertical displacement of material point. Momentarily assuming that v is continuous and using a Taylor series to expand the right-hand-side of eq. (4.2)

$$\theta(\underline{\mathbf{Y}}\langle\xi\rangle, \underline{\mathbf{Y}}\langle-\xi\rangle) \approx \pi - \xi\frac{\partial^2 v}{\partial x^2} + \mathcal{O}(\xi^3)$$

$$\approx \pi - \xi\kappa + \mathcal{O}(\xi^3); \tag{4.3}$$

with

$$\kappa = \frac{\partial^2 v}{\partial x^2}.$$

Substituting eq. (4.3) into the equation for the strain energy density of a single bond-pair,

$$w(\xi) = \omega(\xi)\alpha\left[1 + \cos(\theta(\underline{\mathbf{Y}}\langle\xi\rangle, \underline{\mathbf{Y}}\langle-\xi\rangle))\right]$$

$$\approx \omega(\xi)\alpha\frac{\xi^2}{2}(\kappa)^2 + \mathcal{O}(\xi^4).$$

If we use a weighting function $\omega(\xi) = \omega(|\xi|)$ and assume that the ω plays the role of a localization kernel, i.e. $\omega = 0 \ \forall \ \xi > \delta$, the resulting strain energy density, W, for any material point in the peridynamic beam is

$$W = \frac{\alpha}{2}\kappa^2 \int_{-\delta}^{\delta} \omega(\xi)\xi^2 \mathrm{d}\xi + \mathcal{O}(\delta^5).$$

Equating W with the classical Euler-Bernoulli beam strain-energy density, Ω, and taking the limit as $\delta \to 0$ we can solve for α

$$\lim_{\delta \to 0} W = \Omega,$$

$$\frac{\alpha}{2}m\kappa^2 = \frac{EI}{2}\kappa^2,$$

$$\alpha = \frac{EI}{m}, \tag{4.4}$$

with

$$m = \int_{-\delta}^{\delta} \omega(\xi)\xi^2 \mathrm{d}\xi.$$

31

While this demonstrates the model's equivalence to a linearly-elastic Euler beam, if we keep an additional term from the Taylor series approximation of eq. (4.2), we recover a slightly more complex expressions for change in angle that is demonstrated in 4.2.2 to reproduce an Euler beam governed by Eringen's model of nonlocal elasticity.

4.2.2 Relation to Eringen Nonlocality

If we keep an additional term from the Taylor series approximation of eq. (4.2), we recover a slightly more complex expressions for change in angle

$$\theta(\mathbf{Y}\langle\xi\rangle, \mathbf{Y}\langle-\xi\rangle) \approx \arctan\left(\pi - \xi\frac{\partial^2 v}{\partial x^2} - \frac{\xi^3}{12}\frac{\partial^4 v}{\partial x^4} + \mathcal{O}(\xi^5)\right)$$

and for the strain energy (again substituting $\kappa = v''$ for readability),

$$W \approx \int_{-\delta}^{\delta} \omega(\xi)\alpha(\frac{\xi^2}{2}\kappa^2 + \frac{\xi^4}{12}\kappa\kappa'' - \frac{3}{8}\frac{\xi^4}{8}\kappa^4 + \mathcal{O}(\xi^6))d\xi.$$

As the horizon δ becomes small, higher-order ξ terms become relatively less important, and $\xi^4\kappa^4$ is dominated by $\xi^2\kappa^2$ for large κ and by $\xi^4\kappa\kappa''$ for small κ. The remaining terms can be rearranged,

$$W \approx \int_{-\delta}^{\delta} \omega(\xi)\alpha\frac{\xi^2}{2}\kappa(\kappa + \frac{\xi^2}{6}\kappa'')d\xi,$$

in a manner strongly suggesting an alternative bending resistance term. We can picture a bending resistance based on the bond length and proportional to the nonlocal curvature $\bar{\kappa} = (\kappa + \frac{\xi^2}{6}\kappa'')$, so that

$$\bar{\kappa} = (\kappa + \frac{\xi^2}{6}\kappa'') \implies \tag{4.5}$$
$$W \approx \int_{-\delta}^{\delta} \omega(\xi)\alpha\frac{\xi^2}{2}\kappa\bar{\kappa}d\xi.$$

The same analysis can be taken further to obtain higher-order energy terms with even powers of ξ and even order derivatives of κ. Not all of these higher-order terms can be separated into the product of a local curvature and nonlocal bending resistance.

Eringen's model for nonlocal elasticity in [21] begins with a nonlocal modulus (denoted here as $K(|\mathbf{x}' - \mathbf{x}|, \tau)$) that relates the nonlocal stress $\mathbf{t}$ at a point to the classical (local) stress $\boldsymbol{\sigma}$ in the nearby material through the integral

$$\mathbf{t} = \int_{\mathbf{V}} K(|\mathbf{x}' - \mathbf{x}|, \tau)\boldsymbol{\sigma}(\mathbf{x}')dv(\mathbf{x}').$$

In the local limit these relationships take the form of higher-order gradients. Using a 1-dimensional decaying exponential nonlocal modulus $K(|x|, \tau) = \frac{1}{l\tau}e^{-\frac{|x|}{l\tau}}$ results in a relationship between t_{1D} and σ_{1D}

$$\left(1 - \tau^2 l^2 \frac{\partial^2}{\partial x^2}\right) t_{1D} = \sigma_{1D},$$

in which $\tau^2 l^2$ is a scale-based material parameter. For well-behaved t_{1D} and σ_{1D} and small values of σ_{1D}'''' and $\tau^2 l^2$, we can see that this relationship could be reformulated as

$$t_{1D} = \left(1 + \tau^2 l^2 \frac{\partial^2}{\partial x^2}\right) \sigma_{1D}.$$

If we consider the results of the previous section and let $dM = y\sigma dA$ and $\sigma = Ey\kappa$, the contribution to moment resulting from Eringen's nonlocal elasticity in a fiber at y

$$Ey^2(\kappa + \tau^2 l^2 \kappa''), \tag{4.6}$$

and the resulting strain energy

$$\int_{-\frac{t}{2}}^{\frac{t}{2}} b(y)E\frac{y^2}{2}\kappa(\kappa + \tau^2 l^2 \kappa'')dy,$$

bear a striking resemblance to eq. (4.5). In fact, by carefully choosing peridynamic parameter values, the results can be made identical. For a rectangular beam of width b and thickness t, choosing

$$\omega(\xi) = |\xi|b; \qquad \delta = \tau l \sqrt{3}; \qquad \alpha = \frac{Ebt^3}{54\tau^4 l^4}$$

results in

$$W \approx Eb\frac{t^3}{12}\frac{\kappa}{2}(\kappa + \tau^2 l^2 \kappa''),$$

the same result for both models.

The similarity between eqs. (4.5) and (4.6) is not accidental; Eringen's gradient elasticity is the solution to the integral formulation of the nonlocal stress integral equation just as the peridynamic energy is an integral function of nonlocal displacements. It is therefore unsurprising that, like Eringen's nonlocal elasticity [12], this peridynamic bending model fails to predict the stiffening associated with nanoscale cantilevers. Instead, the advantage of peridynamic models is their natural handling of discontinuities.

4.2.3 Weighting function and inelasticity

The weighting function $\omega(\xi)$ describes the relative contribution of each bond-pair, and can be defined according to physical or mathematical considerations. While any function $\omega(\xi)$ that produces a convergent integral for m will reproduce an elastic Euler beam, a physically meaningful choice of ω will allow us to extend our model to certain inelastic behaviors. Consider a classical Euler-Bernoulli beam in bending with curvature κ. Fibers running parallel to the neutral axis of the beam are stretched in proportion to their distance from the neutral axis, with strain $\epsilon = y\kappa$. If the fibers are linearly elastic, then the axial stress at each location is $\sigma = E\epsilon = Ey\kappa$, and the contribution to supported moment $dM = \kappa Ey^2 dA$. By comparing the formulations for the moments carried by the Euler beam in fig. 4.4 and those of the bond-pair beam in fig. 4.5, we see some definite parallels.
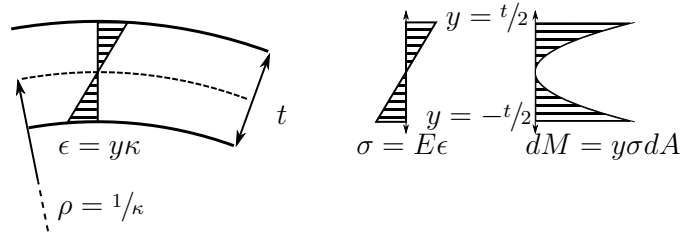
Figure 4.4: Euler beam moment contribution
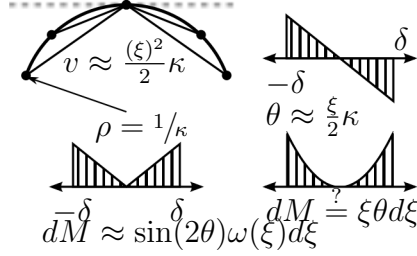
Figure 4.5: Bond-pair moment contribution

$$M_{\mathrm{E}} = \int_{-\frac{t}{2}}^{\frac{t}{2}} \sigma \, y \, dA \qquad\qquad = \int_{-\frac{t}{2}}^{\frac{t}{2}} E\kappa \, y^2 \, b(y) dy$$

$$M_{\mathrm{PD}} = \int_{-\delta}^{\delta} \underline{\mathbf{T}}\langle \xi \rangle \, \xi \, d\xi$$

$$= \int_{-\delta}^{\delta} \alpha \frac{\sin(\Delta\theta)}{|\xi|} \, \xi \, \omega(\xi) d\xi \qquad\qquad \approx \int_{-\delta}^{\delta} \alpha\kappa|\xi| \, \omega(\xi) d\xi$$

The term y is the distance from the beam's neutral axis and $b(y)$ is the width of the beam at that distance from the neutral axis. The similarity between classical and peridynamic moment formulations suggests a possible formulation for the weighting function:

$$\omega(\xi) = |\xi| b\left(y\right) \quad \text{at} \quad y = \frac{\xi}{\delta}\frac{t}{2} \tag{4.7}$$

This weight function analogizes the relative contributions of bond pairs of different lengths to the relative contributions of fibers at different distances from the centerline. An example for a rectangular beam is illustrated in fig. 4.6. For an I beam with height h_{beam}, width w_{beam}, web height
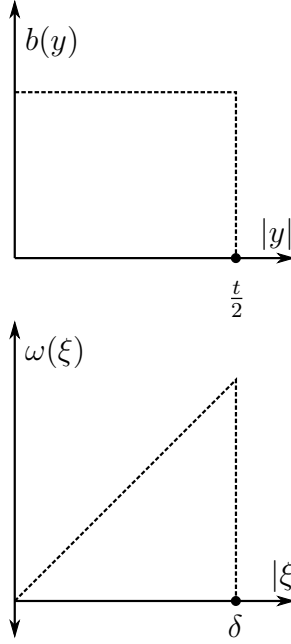
Figure 4.6: Weight function for a beam of rectangular cross-section

h_{web}, and web width w_{web}, substituting the beam profile

$$
b(y) = \begin{cases} w_{\text{web}} & \text{if } |y| \leq \dfrac{h_{\text{web}}}{2} \\[2mm] w_{\text{beam}} & \text{if } \dfrac{h_{\text{web}}}{2} < |y| \leq \dfrac{h_{\text{beam}}}{2} \\[2mm] 0 & \text{otherwise} \end{cases}
$$

into eq. (4.7) gives the weight function

$$
\omega(\xi) = \begin{cases} |\xi| w_{\text{web}} & \text{if } |\xi| \leq \delta \dfrac{h_{\text{web}}}{h_{\text{beam}}} \\[2mm] |\xi| w_{\text{beam}} & \text{if } \delta \dfrac{h_{\text{web}}}{h_{\text{beam}}} < |\xi| \leq \delta \\[2mm] 0 & \text{otherwise} \end{cases}
$$

and is ilustrated in fig. 4.7. While this weighting function offers no advantages over a uniform weight function in the case of the linearly elastic beam, it offers a way to model advancing plasticity.

In a deformed elastic perfectly-plastic beam, axial fibers are still stretched in proportion to their

36
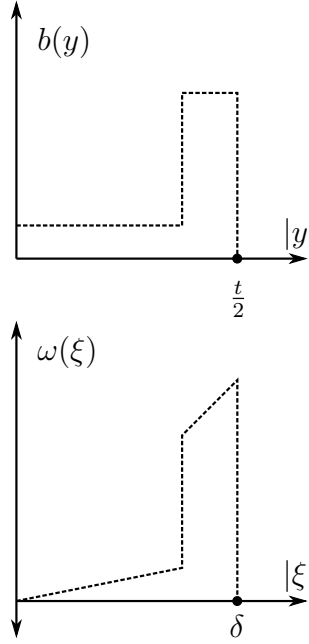
Figure 4.7: Weight function for an I-beam

distance from the neutral axis, but the relationship $\sigma = E\epsilon = Ey\kappa$ only holds for $|\epsilon| = |y\kappa| < \epsilon_c$. For greater stretches, the relationship becomes $\sigma = \pm E\epsilon_c$. To model this behavior, consider a bond pair with similar behavior: for angular deformation less than some critical angle, the model behaves as previously described, but the magnitude of the force remains constant above a critical deformation

$$|\mathbf{T}\langle\xi\rangle| = \begin{cases} \alpha\omega(\xi)\frac{\sin(\theta(\mathbf{Y}\langle\xi\rangle,\mathbf{Y}\langle-\xi\rangle))}{|\mathbf{Y}\langle\xi\rangle|} & \text{if } \theta < \theta_c \\ \alpha\omega(\xi)\frac{\sin(\theta_c)}{|\mathbf{Y}\langle\xi\rangle|} & \text{if } \theta \geq \theta_c \end{cases} \tag{4.8}$$

to determine the critical angle θ_c, we let the onset of plasticity in pairs of the longest bonds to coincide with the onset of plasticity in the fibers at the top and bottom surfaces of the classical beam. For small curvatures $\Delta\theta = \xi\kappa \implies \Delta\theta_c = \frac{2\delta\epsilon_c}{t}$. For curvatures $|\kappa| > \kappa_c = \frac{2\epsilon_c}{t}$, the radius within which bonds are in the elastic region is $\delta_e = \delta\frac{\kappa_c}{\kappa}$, and parallels the distance from the beam

37

centerline that fibers are in the elastic region $y_e = \frac{t}{2}\frac{\kappa_c}{\kappa}$

$$M_{\text{classical}} = 2\int_0^{y_e} Eb(y)y^2\kappa dy + 2\int_{y_e}^{\frac{t}{2}} Eb(y)\epsilon_c y dy$$

$$M_{\text{PD}} = 2\int_0^{\delta_e} \alpha\omega(\xi)\xi^2\kappa d\xi + 2\int_{\delta_e}^{\delta} \alpha\omega(\xi)\Delta\theta_c\xi d\xi$$

Of course, as long as the force is independent of history, this model only represents a nonlinear elastic material. By keeping track of the plastic deformation $\theta^p(\xi) = \theta - \theta_c$ of each bond-pair, and applying it as an offset, we can reproduce the hysteresis associated with elastic-perfectly-plastic deformation.

More simply, we can model a brittle material by setting the force to zero for bond pairs exceeding a critical angle,

$$|\mathbf{T}\langle\xi\rangle| = \begin{cases} \alpha\omega(\xi)\frac{\sin(\theta(\mathbf{Y}\langle\xi\rangle,\mathbf{Y}\langle-\xi\rangle))}{|\mathbf{Y}\langle\xi\rangle|} & \text{if } \theta < \theta_c \\ 0 & \text{if } \theta \geq \theta_c \end{cases} \tag{4.9}$$

and additionally recording bond pairs that have exceeded their critical angle and permanently setting their influence, i.e. ω, to zero.

4.3 Bond Pair Plate in Bending

The next case we will analyze is the extension of the bond pair beam model to fig. 4.8, a flat plate in the xy plane, with displacement in the z-direction.

4.3.1 Energy Equivalence

As with the beam model, we determine an appropriate choice of α so that our peridynamic model will have an equivalent strain energy density to a classical Kirckhoff plate in the *local limit*.. We will begin with the assumptions from Kirckhoff plate theory: straight lines normal to the mid-surface remain both straight and normal to the deformed mid-surface, and the plate thickness does not change with deformation. As with the Euler beam energy equivalence, we will start with the
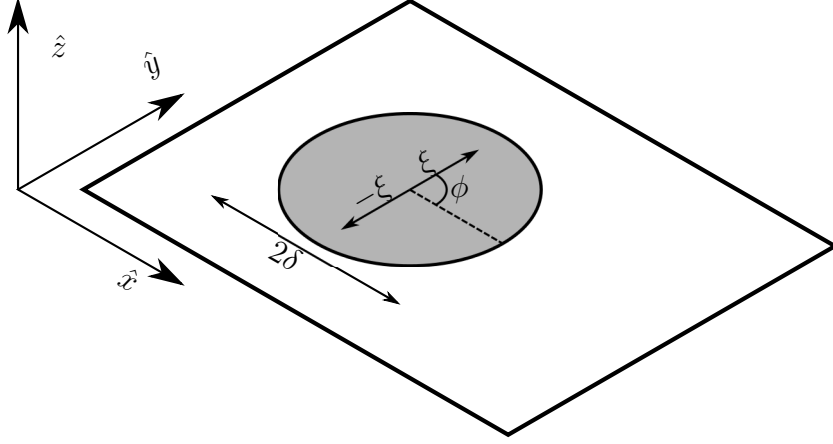
Figure 4.8: Illustration of a bond pair on a plate.

original assumptions from Kirchhoff-Love plate theory of small displacements and rotations, but they will not constrain the validity of the model for larger displacements and rotations. For small vertical displacements we have

$$\theta(\underline{\mathbf{Y}}\langle\boldsymbol{\xi}\rangle, \underline{\mathbf{Y}}\langle-\boldsymbol{\xi}\rangle) \approx \pi - \frac{z(\mathbf{x}+\boldsymbol{\xi}) - 2z(\mathbf{x}) + z(\mathbf{x}-\boldsymbol{\xi})}{|\boldsymbol{\xi}|}, \tag{4.10}$$

where z is the vertical displacement of material point. Taking $\boldsymbol{\xi} = \xi(\cos(\phi), \sin(\phi))$ in cartesian coordinates and momentarily assuming continuous displacements for the sake of comparison, we use a Taylor series to expand the right-hand-side of eq. (4.10) about $\xi = 0$

$$\theta(\underline{\mathbf{Y}}\langle\boldsymbol{\xi}\rangle, \underline{\mathbf{Y}}\langle-\boldsymbol{\xi}\rangle) \approx \pi - \frac{\xi}{2}\left(\cos^2(\phi)\kappa_1 + \sin^2(\phi)\kappa_2 + 2\sin(\phi)\cos(\phi)\kappa_3\right) + \mathcal{O}(\xi^3) \tag{4.11}$$

with

$$\kappa_1 = \frac{\partial^2 z}{\partial x_1^2}, \quad \kappa_2 = \frac{\partial^2 z}{\partial x_2^2}, \quad \kappa_3 = \frac{\partial^2 z}{\partial x_1 \partial x_2}$$

substituting eq. (4.11) into the equation for the strain energy density of a single bond-pair,

$$w = \omega(\boldsymbol{\xi})\alpha\left[1 + \cos(\theta(\mathbf{Y}\langle\boldsymbol{\xi}\rangle, \mathbf{Y}\langle-\boldsymbol{\xi}\rangle))\right]$$

$$= \omega(\boldsymbol{\xi})\alpha\frac{\xi^2}{8}(\kappa_1^2\cos^4(\phi) + \kappa_2^2\sin^4(\phi) + 2\kappa_1\kappa_2\cos^2(\phi)\sin^2(\phi) + 4\kappa_3^2\cos^2(\phi)\sin^2(\phi)$$

$$+ 4\kappa_1\kappa_3\cos^3(\phi)\sin(\phi) + 4\kappa_2\kappa_3\cos(\phi)\sin^3(\phi)) + \mathcal{O}(\xi^4).$$

If we use a weighting function $\omega(\boldsymbol{\xi}) = \omega(\xi)$ and assume that the ω plays the role of a localization kernel, i.e. $\omega = 0 \ \forall \ \xi > \delta$, the resulting strain energy density, W, for any material point in the peridynamic plate is

$$W = \alpha\int_0^\delta\int_0^{2\pi} w\,\xi\mathrm{d}\phi\mathrm{d}\xi,$$

$$= \alpha\frac{3\pi}{8}\left(\kappa_1^2 + \kappa_2^2 + \frac{2}{3}\kappa_1\kappa_1 + \frac{4}{3}\kappa_3^2\right)\int_0^\delta\omega(\xi)\xi^3\mathrm{d}\xi + \mathcal{O}(\delta^6).$$

Equating W with the classical Kirchhoff plate strain-energy density, Ω, and taking the limit as $\delta \to 0$ we can solve for α

$$\lim_{\delta\to 0} W = \Omega,$$

$$\alpha\frac{3\pi}{8}m\left(\kappa_1^2 + \kappa_2^2 + \frac{2}{3}\kappa_1\kappa_1 + \frac{4}{3}\kappa_3^2\right) = \left[\frac{Gh^3}{12(1-\nu)}\left(\kappa_1^2 + \kappa_2^2 + 2\nu\kappa_1\kappa_1 + 2(1-\nu)\kappa_3^2\right)\right]_{\nu=1/3},$$

$$\alpha = \frac{2Gh^3}{3m}, \tag{4.12}$$

with

$$m = \int_0^\delta\int_0^{2\pi}\omega(\xi)\xi^2\xi\mathrm{d}\phi\mathrm{d}\xi,$$

where G is the shear modulus, h is the thickness of the plate, and we have evaluated the classical Kirchhoff strain-energy at a Poisson ratio of $1/3$ in order to solve for alpha as a constant. Because α is inversely proportional to m, the energy does not change with varying choices for ω and δ. It should be noted that the restriction $\nu = 1/3$ is the same imposed by the use of a bond based

peridynamic model for in-plane deformation of a 2D peridynamic plate. We will show an extension to this model that removes this restriction in Section 4.4.

4.3.2 Combining Bending and Extension Models

The bond-pair bending model does not resist in-plane stretching or shear deformation because these deformations preserve the angles between opposite bonds. If these behaviors are expected in combination with bending, a useful model must resist both in-plane and transverse deformations. To create a plate model that also resists these deformations, i.e. a flat shell, we combine the bond-pair model with a two-dimensional version of the original bond-based linearly-elastic peridynamic solid model from [62]. In this model, individual bonds act as springs resisting changes in length.

$$\underline{\mathbf{T}}\langle \boldsymbol{\xi} \rangle = \beta \left(|\underline{\mathbf{Y}}\langle \boldsymbol{\xi} \rangle| - |\boldsymbol{\xi}| \right) \frac{\underline{\mathbf{Y}}\langle \boldsymbol{\xi} \rangle}{|\underline{\mathbf{Y}}\langle \boldsymbol{\xi} \rangle|} \tag{4.13}$$

By matching the energy of a 2D material in shear deformation, we can relate β to the shear modulus and thickness of the shell. Following the example of [64], we begin with a 2D material under pure in-plane shear. In Einstein notation, the strain energy of this material is

$$W_{\mathrm{C}} = G \, h \, \epsilon_{ij}^{d} \epsilon_{ij}^{d},$$

$$\begin{aligned}
W_{\mathrm{PD}} &= \frac{\beta}{2} \int_{A} \omega(\xi) \left(|\underline{\mathbf{Y}}\langle \boldsymbol{\xi} \rangle| - |\boldsymbol{\xi}| \right)^{2} \, \mathrm{d}A_{\boldsymbol{\xi}}, \\
&= \frac{\beta}{2} \int_{A} \omega(\xi) \frac{\epsilon_{ij}\xi_i\xi_j}{|\boldsymbol{\xi}|} \frac{\epsilon_{kl}\xi_k\xi_l}{|\boldsymbol{\xi}|} \, \mathrm{d}A_{\boldsymbol{\xi}}, \\
&= \frac{\beta}{2} \epsilon_{ij}^{d} \epsilon_{kl}^{d} \int_{A} \frac{\omega(\xi)}{|\boldsymbol{\xi}|^2} \xi_i\xi_j\xi_k\xi_l \, \mathrm{d}A_{\boldsymbol{\xi}}.
\end{aligned}$$

where ϵ^{d} is the deviatoric strain tensor. Now, to evaluate the integral we will exploit the symmetry properties. With $i, j, k, l = 1, 2$. For a circular $\omega(\xi) = \omega(|\xi|)$, combinations of $\{i, j, k, l\}$ with an odd number of each index, such as $\{1, 1, 1, 2\}$ or $\{2, 1, 2, 2\}$, will result in odd powers of sine and
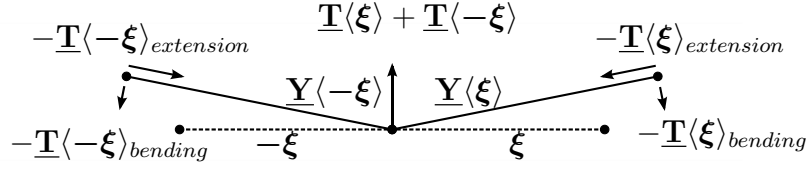
Figure 4.9: The Hybrid Model Combines Bending and Extension Components

cosine and integrate to 0.

$$m = \int_A \omega(\xi)|\boldsymbol{\xi}|^2 \, dA_{\boldsymbol{\xi}}$$

$$W_{\text{PD}}^d = \frac{\beta \, m}{16}[3(\epsilon_{11}\epsilon_{11} + \epsilon_{22}\epsilon_{22}) + (\epsilon_{11}\epsilon_{22} + \epsilon_{12}\epsilon_{12} + \epsilon_{12}\epsilon_{21} + \epsilon_{21}\epsilon_{12} + \epsilon_{21}\epsilon_{21} + \epsilon_{22}\epsilon_{11})]$$

$$= \frac{\beta \, m}{16}\epsilon_{ij}^d\epsilon_{kl}^d(\delta_{ij}\delta_{kl} + \delta_{ik}\delta_{jl} + \delta_{il}\delta_{jk})$$

$$= \frac{\beta \, m}{8}\epsilon_{ij}^d\epsilon_{ij}^d \implies$$

$$\beta = \frac{8 \, G \, h}{m}$$

Having calibrated the bond-extension model to the shear modulus for a case of pure in-plane shear, applying a different uniform strain (such as might result from uniaxial tension) reveals the bond-based model to result in a one-parameter linearly-elastic model with Poisson's ratio $\nu = {}^1\!/_3$.

Combining the bending and extension models allows for the description of more complex behaviors, particularly the stiffening effect of in-plane tension on the transverse bending of a shell. Consider a single bond-pair in the combined model shown in Fig. 4.9. As the two sides are pulled apart, the magnitude of the extension force in each bond increases, and the magnitude of the bending force decreases. At the same time, the angle at which the extension force acts decreases, and the angle of action for the bending force increases. For small amounts of bending and reasonable stretches, increased tension in the direction of the bond pair results in increased restorative force.

4.4 Extension to arbitrary Poisson ratio

Although many materials have Poisson ratios of $\nu \approx 1/3$, it is nonetheless desirable to extend the model to materials with arbitrary Poisson ratios. For isotropic, linearly elastic models of solid materials, Silling et al. extended the peridynamic material model to arbitrary material parameters in [64] by decomposing the deformation into isotropic and deviatoric components. In the absence of plastic deformation, we need only find the difference between the strain energy of a deformed bond-based plate and the strain energy of an elastic plate with Poisson's ratio $\nu \neq 1/3$. The difference is a function of the isotropic strain in two dimensions, θ_2

$$W' = \frac{G\,h}{2} \left(\frac{3\nu - 1}{1 - \nu} \right) \theta_2^2$$

$$\theta_2 = \frac{2}{m} \int_A \omega(\boldsymbol{\xi}) |\boldsymbol{\xi}| (|\underline{\mathbf{Y}}\langle \boldsymbol{\xi} \rangle| - |\boldsymbol{\xi}|) \, dA_{\boldsymbol{\xi}}$$

$$W_{\text{total}} = \frac{G\,h}{2} \left(\frac{3\nu - 1}{1 - \nu} \right) \theta_2^2 + \frac{4\,G\,h}{m} \int_A \omega(\boldsymbol{\xi}) (|\underline{\mathbf{Y}}\langle \boldsymbol{\xi} \rangle| - |\boldsymbol{\xi}|)^2 \, dA_{\boldsymbol{\xi}}$$

This is to be expected because the bond-based model was calibrated to the shear strain energy, leaving discrepancies proportional to the isotropic strain energy that fall to 0 as Poisson's ratio approaches $\nu = 1/3$.

This decomposition method inspires a similar approach to our plate model. To perform the same extension for the plate model in bending, we find the error in the 1-parameter strain energy for $\nu \neq 1/3$

$$W' = \frac{Gh^3}{12(1 - \nu)} \left(\kappa_1^2 + \kappa_2^2 + 2\nu\kappa_1\kappa_2 + 2(1 - \nu)\kappa_3^2 \right)$$

$$- \frac{Gh^3}{12(1 - \frac{1}{3})} \left(\kappa_1^2 + \kappa_2^2 + \frac{2}{3}\nu\kappa_1\kappa_2 + 2(1 - \frac{1}{3})\kappa_3^2 \right)$$

$$W' = 2G \frac{h^3}{12} \frac{3\nu - 1}{1 - \nu} \left(\frac{\kappa_1 + \kappa_2}{2} \right)^2.$$

The discrepancy in energy is proportional to the square of average curvature, $\frac{\kappa_1 + \kappa_2}{2} = \bar{\kappa}$, which we will also refer to as the isotropic curvature. The isotropic curvature can be envisioned as the

portion of the deformation that resembles a hemispherical bowl. The remainder of the bending deformation, that which is left when the isotropic curvature is subtracted out, resembles a saddle. This remaining component is the deviatoric deformation, and both components are shown in fig. 4.10. Note that the orientation of the deviatoric bending will change depending on the particular curvature being decomposed, while the isotropic curvature will only change in scale. A
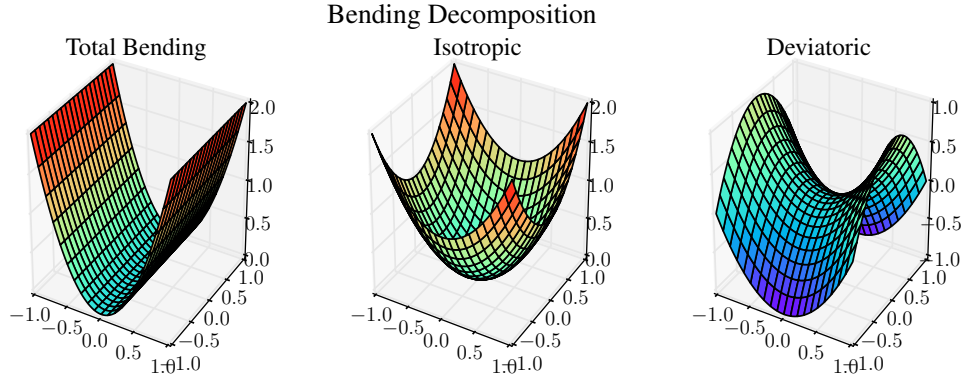
Figure 4.10: Bending Deformation Decomposed into Isotropic and Deviatoric Portions

complete decomposition of bending energy into isotropic and deviatoric components as performed by Fischer in [24] produces a far more complex model and is unnecessary at this time. For a single bond pair we can represent the curvature vector along the bond pair as

$$\boldsymbol{\kappa}_{\hat{\boldsymbol{\xi}}} = \frac{\mathbf{\underline{Y}}\langle\boldsymbol{\xi}\rangle + \mathbf{\underline{Y}}\langle-\boldsymbol{\xi}\rangle}{|\boldsymbol{\xi}|^2}$$

For large rotations, we can define an average curvature vector $\bar{\boldsymbol{\kappa}}$. This leads us to model the average curvature as

$$\bar{\boldsymbol{\kappa}} = \frac{1}{m} \int_0^\delta \int_0^{2\pi} \omega(\xi) \frac{\mathbf{\underline{Y}}\langle\boldsymbol{\xi}\rangle + \mathbf{\underline{Y}}\langle-\boldsymbol{\xi}\rangle}{\xi^2} \xi \mathrm{d}\phi \mathrm{d}\xi;$$
$$m = \int_0^\delta \int_0^{2\pi} \omega(\xi) \xi \mathrm{d}\phi \mathrm{d}\xi.$$

The weighting function $\omega(\xi)$ performs the same function as in the previous section. We can rewrite

44

the energy discrepancy in terms of $\bar{\boldsymbol{\kappa}}$.

$$W' = 2G\frac{h^3}{12}\frac{3\nu - 1}{1 - \nu}\bar{\boldsymbol{\kappa}}^2.$$

We can take the Fréchet derivative (details in A) to produce a correction force vector state

$$\underline{\mathbf{T}}'\langle\boldsymbol{\xi}\rangle = \frac{8G}{m}\frac{h^3}{12}\frac{3\nu - 1}{1 - \nu}\frac{\omega(\boldsymbol{\xi})}{\xi^2}\bar{\boldsymbol{\kappa}}, \tag{4.14}$$

that is not directly dependent on the deformation of a single bond pair. Instead, eq. (4.14) represents a bond-length dependent "pressure" applied to every pair of bonds extending from a node. This "pressure" is proportional to the curvature vector at that node. A weighting function $\omega(\boldsymbol{\xi}) = |\boldsymbol{\xi}|$ can ensure that the integral expression for force at a point is convergent. This extra term that is dependent on the bending of all the pairs around a material point means that the extension is not properly a *bond-pair* model. Instead, it would be more accurate to call it a *bond-multiple* model, in which the bond forces and energies are functions of the relationship between a family of bonds. In either the continuous or discrete cases, this model extension requires the additional step of evaluating the isotropic curvature at each point, but the increased complexity of the extended model captures in the local limit the behavior of a two-parameter elastic material plate.

Chapter 5: NUMERICAL SIMULATION

5.1 Discretized Bond Pair Beam

Discretizing the bond-pair model is primarily matter of exchanging integrals for sums.

$$w(\boldsymbol{\xi}_i) = \omega(\boldsymbol{\xi}_i)\alpha \left[1 + \cos(\theta(\underline{\mathbf{Y}}\langle\boldsymbol{\xi}_i\rangle, \underline{\mathbf{Y}}\langle-\boldsymbol{\xi}_i\rangle))\right]$$

$$\approx \omega(\boldsymbol{\xi}_i)\frac{\alpha}{2}\left(\frac{v(\mathbf{x}+\boldsymbol{\xi}_i) - 2v(\mathbf{x}) + v(\mathbf{x}-\boldsymbol{\xi}_i)}{\boldsymbol{\xi}_i}\right)^2$$

in which $\boldsymbol{\xi}_i$ is the ith bond emanating from the point $\mathbf{x}$ to each of the n points within distance δ of point $\mathbf{x}$.

$$\alpha = \frac{c\,\Delta x}{m}; \ c = EI; \ m = \sum_{i=1}^{n}\omega(\boldsymbol{\xi}_i)\boldsymbol{\xi}_i^2 \implies$$

$$W = \Delta x \sum_{i=1}^{n}\frac{EI}{2}\omega(\boldsymbol{\xi}_i)\left(\frac{v(\mathbf{x}+\boldsymbol{\xi}_i) - 2v(\mathbf{x}) + v(\mathbf{x}-\boldsymbol{\xi}_i)}{\boldsymbol{\xi}_i}\right)^2$$

Discretization of the original model results in the equation of motion

$$\rho(\mathbf{x})\ddot{\mathbf{u}}(\mathbf{x}) = \mathbf{f}(\mathbf{x}) + \sum_i \omega(\boldsymbol{\xi}_i)\left\{\frac{\alpha(\mathbf{x})}{|\mathbf{p}_i|}\frac{\mathbf{p}_i}{|\mathbf{p}_i|} \times \left[\frac{\mathbf{p}_i}{|\mathbf{p}_i|} \times \frac{\mathbf{q}_i}{|\mathbf{q}_i|}\right]\right.$$
$$\left. -\frac{\alpha(\mathbf{x}+\boldsymbol{\xi}_i)}{|\mathbf{p}_i|}\frac{(-\mathbf{p}_i)}{|\mathbf{p}_i|} \times \left[\frac{(-\mathbf{p}_i)}{|\mathbf{p}_i|} \times \frac{\mathbf{r}_i}{|\mathbf{r}_i|}\right]\right\} \tag{5.1}$$

with

$$\mathbf{p}_i = \boldsymbol{\xi}_i + \mathbf{u}(\mathbf{x}+\boldsymbol{\xi}_i) - \mathbf{u}(\mathbf{x});$$

$$\mathbf{q}_i = -\boldsymbol{\xi}_i + \mathbf{u}(\mathbf{x}-\boldsymbol{\xi}_i) - \mathbf{u}(\mathbf{x});$$

$$\mathbf{r}_i = \boldsymbol{\xi}_i + \mathbf{u}(\mathbf{x}+2\boldsymbol{\xi}_i) - \mathbf{u}(\mathbf{x}+\boldsymbol{\xi}_i).$$

and for small displacements and rotations in a uniform beam,

$$
\begin{aligned}
\rho(\mathbf{x})\ddot{v}(\mathbf{x}) = {} & f(\mathbf{x}) \\
& + \alpha \sum_i 2\omega(\xi_i) \left(\frac{v(\mathbf{x} - 2\boldsymbol{\xi}_i) - 4v(\mathbf{x} - \boldsymbol{\xi}_i) + 6v(\mathbf{x}) - 4v(\mathbf{x} + \boldsymbol{\xi}_i) + v(\mathbf{x} + 2\boldsymbol{\xi}_i)}{\boldsymbol{\xi}_i^2} \right)
\end{aligned}
$$

It is worth noting the similarity between this expression and a finite-difference fourth derivative of displacement, a result expected from Euler beam theory. This discretization requires that nodes be evenly spaced along the entire beam, otherwise the displacement $v(\mathbf{x} - \boldsymbol{\xi}_i)$ is ill-defined. For this reason, the discretization does not allow for areas of higher and lower "resolution".

5.2   Discretized Bond Pair Plate
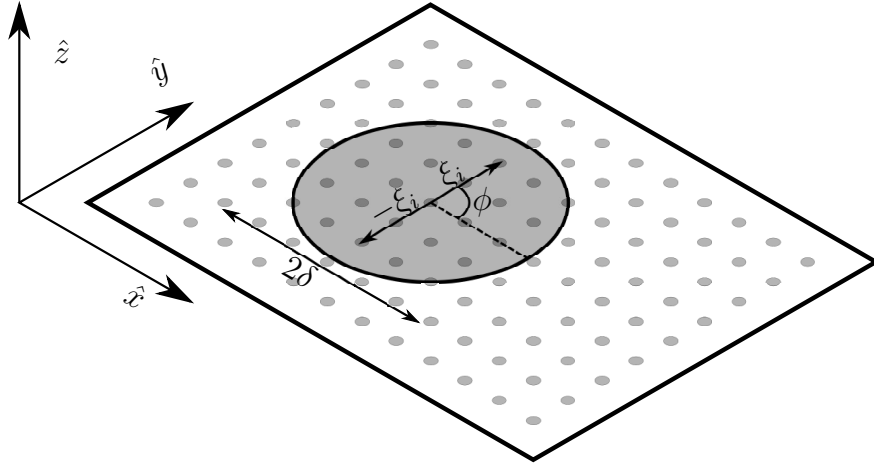
Figure 5.1: Discretized peridynamic plate with illustrated bond pair

As with the beam, discretizing the bond-pair model is primarily matter of exchanging integrals

for sums.

$$\alpha = \frac{c\,(\Delta x)^2}{m}; \ c = \frac{G}{(1-\nu)}\frac{h^3}{12}; \ m = \sum_{i=1}^{n}\omega(\boldsymbol{\xi}_i)\boldsymbol{\xi}_i^2 \implies$$

$$W = (\Delta x)^2 \sum_{i=1}^{n}\omega(\boldsymbol{\xi}_i)\frac{G}{2(1-\nu)}\frac{h^3}{12}\left(\frac{z(\mathbf{x}+\boldsymbol{\xi}_i) - 2z(\mathbf{x}) + z(\mathbf{x}-\boldsymbol{\xi}_i)}{|\boldsymbol{\xi}_i|}\right)^2$$

Discretization of the 1-parameter bending model results in the same equation of motion as for the beam model (eq. 5.1).

Implementing the 2-parameter model requires finding the isotropic curvature at each point.

$$\bar{\boldsymbol{\kappa}}(\mathbf{x}) = \frac{1}{m}\sum_{i}\omega(\boldsymbol{\xi}_i)\frac{\mathbf{p}_i + \mathbf{q}_i}{\boldsymbol{\xi}_i^2};$$

$$m(\mathbf{x}) = \sum_{i}\omega(\boldsymbol{\xi}_i);$$

$$\alpha^{\text{iso}}(\mathbf{x}) = \frac{4G}{m}\frac{h^3}{12}\frac{3\nu - 1}{1 - \nu}(\Delta x)^2;$$

$$f^{\text{iso}}(\mathbf{x}) = \sum_{j}\left\{\left[\alpha^{\text{iso}}(\mathbf{x})\bar{\boldsymbol{\kappa}}(\mathbf{x}) - \alpha^{\text{iso}}(\mathbf{x}+\boldsymbol{\xi}_j)\bar{\boldsymbol{\kappa}}(\mathbf{x}+\boldsymbol{\xi}_j)\right]\frac{\omega(\boldsymbol{\xi}_j)}{\boldsymbol{\xi}_j^2}\right\}$$

As with the discretized beam, the discretization of the bond-pair plate (fig. 5.1) must be absolutely regular. Discretizing the bond-pair model as proposed above requires that nodes be evenly spaced, Δx, throughout the entire plate, otherwise the displacement $z(\mathbf{x} - \boldsymbol{\xi}_i)$ is undefined. For this reason, the discretization does not allow for areas of higher and lower "resolution". This restriction, while inconvenient in the 1D case, is fairly restricting for plate analysis. An extension to this discretization that would allow changing mesh resolution will require interpolation between the nodes.

5.2.1 Curved Shapes

On a curved surface, the location of the point $\mathbf{x} - \boldsymbol{\xi}$ might be off of the surface entirely. One method of applying the bond-pair model to curved surfaces is through the use of "virtual" points. These points have no mass and do not have families of peridynamic neighbors, they only allow the
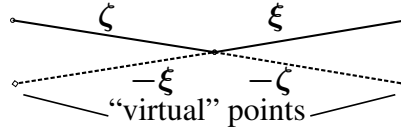
Figure 5.2: Virtual Points Allow Straight Pairs on Curved Surfaces
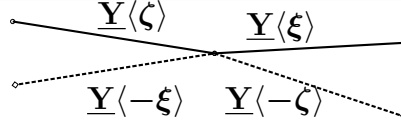
Figure 5.3: Virtual Points Take the Displacement of Nearby Real Points

definition of bond pairs that are straight in the undeformed configuration. In the simplest method,

each virtual point is located just above or below a real point in the model. In this case, properties

such as displacement are taken to be the same as for the nearby real point. Because the virtual

point has no mass is not part of any other bond pairs, it cannot be assigned a force. Instead, the

force on a virtual point resulting from deformation of a bond pair is instead applied to the nearest

real points. This results in a straightforward extension of the bending model from flat plates (and

beams) to features that have curvatures that are small over the peridynamic horizon.

5.2.2 Irregular Discretization

A curved surface is not the only reason to implement virtual points, and even many curved surfaces

do not allow for regular discretization. When discretization is irregular, due to three-dimensional

curvature, irregular shapes, or a need for increased resolution in some areas, there are necessarily

points at which there is no real point at the location of $\mathbf{x} - \boldsymbol{\xi}$. An example of changing mesh

density resulting in a need for interpolation can be found in fig. 5.4, which shows a small family

of nodes at the edge of a change in discretization coarseness. Note that, while bonds p_2 and q_2

form a perfect bond pair, there is no bond exactly opposite p_1. To solve this, we add a virtual

point to create a bond, q_1, that will form a pair with p_1. Because this point is not part of the
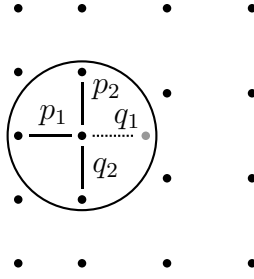
Figure 5.4: Virtual Points Pair Up Unpaired Neighbors
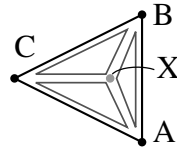
Figure 5.5: Barycentric interpolation is based on the relative areas of sub triangles

discretization, it has no mass, and its properties must be determined from the properties of the surrounding nodes. An easy method of determining properties (such as displacement) at virtual nodes is to use a weighted average. One method of generating useful weights that is relatively robust is barycentric interpolation. We start by finding the three (non-colinear) real nodes closest to the location of the virtual node, A, B, and C. Next, we find the signed areas of the triangles ABC, ABX, BCX, and CAX, with X being the virtual node. The weight of node A is the area ratio between BCX and ABC, the weight of node B is the ratio of areas CAX and ABC, and the weight of node C is the ratio of areas ABX to ABC. Using signed areas allows the weights to be negative to extrapolate properties of a virtual node outside of ABC. Because these weights are calculated from the initial positions of the node, they can be stored for swift evaluation of properties at virtual nodes.

With the properties of the virtual points determined, the model can be evaluated in the same manner as the uniformly discretized models of the previous papers. Where forces are calculated to act on a virtual node, those forces are redistributed to the supporting real nodes according to the weight each point has in the interpolation.

The same method of virtual nodes also allows the modeling of curved surfaces, in which the perfect opposite of a bond may not lie near but not on the surface of the plate or shell. As long as the curvature of the surface is small (at the scale of the peridynamic horizon), each resulting virtual nodes will be nearly in the plane formed by its nearest neighbors. Finding the weights of the surrounding nodes is performed just as in the planar case, except that the areas are formed between the projection of the virtual node location X onto the plane formed by A, B, and C.

To compute the weight of node A in the interpolation of properties at virtual node X, let AB represent the vector from node A to node B, and use

$$W_A' = \frac{B - X}{2} \bullet \left[BC \times \left(\frac{BC \times BA}{|BC \times BA|} \right) \right] \tag{5.2}$$

After finding W_B' and W_C' in similar fashion,

$$W_A = \frac{W_A'}{W_A' + W_B' + W_C'} \tag{5.3}$$

If the projection of X onto the plane defined by A, B, and C lies outside the triangle ABC, one or two of W_A, W_B and W_C will be negative, though they will still sum to 1.

5.3 "Boundary" Conditions

Because peridynamic models result in long range forces, it is not sufficient to apply boundary conditions to nodes on the relevant boundary; nodes near the boundary must be considered as well. For the peridynamic beam we consider applied forces, simple supports or rollers, and fixed or clamped supports. Simply-supported beams are easy to model because only displacement is constrained. To add a roller support to the peridynamic beam, it suffices to constrain the movement of the nearest peridynamic node in the appropriate degree(s) of freedom. Simulating a "clamped" end condition is a little less intuitive. The most basic way to simulate a clamped end is to extend the beam 2δ, or twice the horizon, into the clamp. The displacement of all of those nodes is set
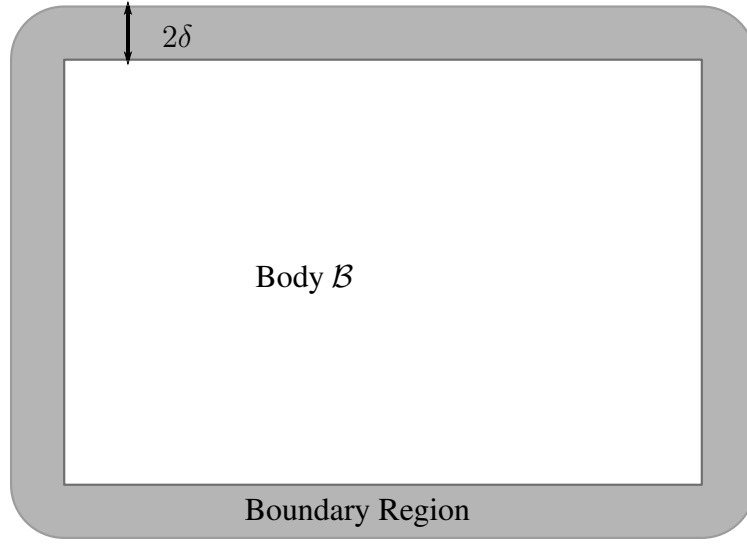
Figure 5.6: The boundary of a peridynamic model is a region of nonzero thickness

to zero, or whatever value is appropriate for a displaced or rotated clamp. In classical mechanics, a clamped end can be described with a symmetry condition, but the two are not peridynamically equivalent. Because the classical beam is a local model, material at a clamp cannot "see" distant material, so there is no way to distinguish between a beam end that is clamped and one that is bent symmetrically over an appropriate sawhorse. Distributed forces may be applied as expected to nodes in the loaded region. Point forces may often be applied directly to the nearest node, or to the nodes immediately surrounding the point of application. Point moments must also be considered more carefully because the peridynamic models in this work, like most peridynamic models, do not consider rotational degrees of freedom for peridynamic nodes. It is therefore impossible to apply a moment to a single peridynamic point. Instead, moments may be applied as force couples to the bonds attached to the peridynamic node nearest the location of the desired moment. For example, if we want to apply a moment M at point $\mathbf{x}$, whose n neighboring points $\mathbf{x}_i'$ are connected to $\mathbf{x}$ in the undeformed configuration by bonds $\boldsymbol{\xi}_i$. For an evenly discretized beam, we may distribute the moments by

$$\mathbf{M}_i = \mathbf{M} \frac{\omega(\boldsymbol{\xi}_i)}{\sum\limits_{j=1}^{n} \omega(\boldsymbol{\xi}_j)}$$

and apply them to the corresponding bonds by adding forces

$$\mathbf{F}_i = \mathbf{M}_i \times \frac{\underline{\mathbf{Y}}\langle\boldsymbol{\xi}_i\rangle}{|\underline{\mathbf{Y}}\langle\boldsymbol{\xi}_i\rangle|^2}$$

to each point $\mathbf{x}_i$ and subtracting them from the force at $\mathbf{x}$.

Support configurations are similar for two-dimensional models. Each node along a simply-supported edge is constrained in one or more directions. As with the beam model, clamped edges are implemented by extending the surface into the clamp. Line and pressure loads are treated normally.

5.4   Numerical Solution Method

This project uses Trilinos, a collection of open software libraries, or packages, from Sandia National Labs, including:

- Epetra and EpetraExt - provide efficient parallel data structures, particularly vectors and sparse matrices

- Isorropia - provides load balancing, partitioning, and matrix coloring

- NOX - a collection of large-scale nonlinear system solver utilities

- PyTrilinos - a python interface providing Python wrappers for many Trilinos packages, and offering compatibility between numpy.ndarrays and Epetra.MultiVectors

The nature of discrete peridynamic models results in large numbers of parallelizable computations. Efficient parallelization is achieved using Epetra data structures for distributed variables. Model force evaluations are coded in Python, making extensive use of the optimized routines in the NumPy and SciPy packages operating on the distributed Epetra objects. To obtain quasistatic solutions, problems are coded into NOX objects and solved using NOX nonlinear solvers. Preliminary analysis was performed using a Newton Method solver on an iMac with a 3.1GHz Intel

Core i7 processor and 16GB RAM, using 1-4 cores. Later work also performed on Shamu, a High-Performance Computing cluster at UTSA. The nature of the Trilinos packages and the structure of the code allow for more extensive parallel computation without major code changes.

For all but the simplest loading conditions, analytical solutions to boundary condition problems become complicated. As load conditions and material behavior become more complex, there are no analytical solutions. For comparison, equivalent models are created and analyzed in Abaqus 6.12 to verify simple cases.

BIBLIOGRAPHY

[1] R Ansari, S Sahmani, and B Arash. Nonlocal plate model for free vibrations of single-layered graphene sheets. *Physics Letters A*, 375(1):53–62, 2010.

[2] Douglas N Arnold. An interior penalty finite element method with discontinuous elements. *SIAM journal on numerical analysis*, 19(4):742–760, 1982.

[3] E. Askari, F. Bobaru, RB Lehoucq, ML Parks, SA Silling, and O. Weckner. Peridynamics for multiscale materials modeling. In *Journal of Physics: Conference Series*, volume 125, page 012078. IOP Publishing, 2008.

[4] Zdenek P Bazant and Ta-Peng Chang. Nonlocal finite element analysis of strain-softening solids. *Journal of engineering mechanics*, 113(1):89–105, 1987.

[5] Zdenek P Bazant and Gilles Pijaudier-Cabot. Nonlocal continuum damage, localization instability and convergence. *Journal of Applied Mechanics*, 55(2):287–293, 1988.

[6] Ted Belytschko and Tom Black. Elastic crack growth in finite elements with minimal remeshing. *International journal for numerical methods in engineering*, 45(5):601–620, 1999.

[7] W Benz and E Asphaug. Simulations of brittle solids using smooth particle hydrodynamics. *Computer physics communications*, 87(1):253–265, 1995.

[8] Florin Bobaru. Influence of van der waals forces on increasing the strength and toughness in dynamic fracture of nanofibre networks: a peridynamic approach. *Modelling and Simulation in Materials Science and Engineering*, 15(5):397, 2007.

[9] Florin Bobaru and Monchai Duangpanya. The peridynamic formulation for transient heat conduction. *International Journal of Heat and Mass Transfer*, 53(19):4047–4059, 2010.

[10] Nathanial Burch and Richard Lehoucq. Classical, nonlocal, and fractional diffusion equations on bounded domains. *International Journal for Multiscale Computational Engineering*, 9(6), 2011.

[11] J Burghardt, R Brannon, and J Guilkey. A nonlocal plasticity formulation for the material point method. *Computer Methods in Applied Mechanics and Engineering*, 225:55–64, 2012.

[12] N Challamel and C M Wang. The small length scale effect for a non-local cantilever beam: a paradox solved. *Nanotechnology*, 19(34):345703, 2008.

[13] RJ Cheng and Kim Meow Liew. Analyzing two-dimensional sine–gordon equation with the mesh-free reproducing kernel particle ritz method. *Computer methods in applied mechanics and engineering*, 245:132–143, 2012.

[14] Gianluca Cusatis, Andrea Mencarelli, Daniele Pelessone, and James Baylot. Lattice discrete particle model (ldpm) for failure behavior of concrete. ii: Calibration and validation. *Cement and Concrete Composites*, 33(9):891–905, 2011.

[15] Gianluca Cusatis, Daniele Pelessone, and Andrea Mencarelli. Lattice discrete particle model (ldpm) for failure behavior of concrete. i: Theory. *Cement and Concrete Composites*, 33(9):881–890, 2011.

[16] Kaushik Dayal and Kaushik Bhattacharya. Kinetics of phase transformations in the peridynamic formulation of continuum mechanics. *Journal of the Mechanics and Physics of Solids*, 54(9):1811–1842, 2006.

[17] Paul N Demmie and Stewart A Silling. An approach to modeling extreme loading of structures using peridynamics. *Journal of Mechanics of Materials and Structures*, 2(10):1921–1945, 2007.

[18] John Dolbow, Nicolas Moës, and Ted Belytschko. Modeling fracture in mindlin–reissner plates with the extended finite element method. *International Journal of Solids and Structures*, 37(48):7161–7183, 2000.

[19] WH Duan and CM Wang. Exact solutions for axisymmetric bending of micro/nanoscale circular plates based on nonlocal plate theory. *Nanotechnology*, 18(38):385704, 2007.

[20] Etienne Emmrich and Olaf Weckner. Analysis and numerical approximation of an integro-differential equation modeling non-local effects in linear elasticity. *Mathematics and Mechanics of Solids*, 12(4):363–384, 2007.

[21] A Cemal Eringen. On differential equations of nonlocal elasticity and solutions of screw dislocation and surface waves. *Journal of Applied Physics*, 54(9):4703–4710, 1983.

[22] A.C. Eringen and DGB Edelen. On nonlocal elasticity. *International Journal of Engineering Science*, 10(3):233–248, 1972.

[23] XJ Fang, QD Yang, BN Cox, and ZQ Zhou. An augmented cohesive zone element for arbitrary crack coalescence and bifurcation in heterogeneous materials. *International Journal for Numerical Methods in Engineering*, 88(9):841–861, 2011.

[24] Thomas M Fischer. Bending stiffness of lipid bilayers. iii. gaussian curvature. *Journal de Physique II*, 2(3):337–343, 1992.

[25] John Foster, Stewart A. Silling, and Weinong Chen. An energy based failure criterion for use with peridynamic states. *International Journal for Multiscale Computational Engineering*, 9(6):675–988, 2011.

[26] JT Foster, SA Silling, and WW Chen. Viscoplasticity using peridynamics. *International Journal for Numerical Methods in Engineering*, 81(10):1242–1258, 2010.

[27] JW Foulk, DH Allen, and KLE Helms. Formulation of a three-dimensional cohesive zone model for application to a finite element algorithm. *Computer methods in applied mechanics and engineering*, 183(1):51–66, 2000.

[28] Thomas-Peter Fries and Ted Belytschko. The extended/generalized finite element method: an overview of the method and its applications. *International Journal for Numerical Methods in Engineering*, 84(3):253–304, 2010.

[29] Walter Gerstle, Nicolas Sau, and Stewart Silling. Peridynamic modeling of concrete structures. *Nuclear engineering and design*, 237(12):1250–1258, 2007.

[30] PC Guan, JS Chen, Y Wu, H Teng, J Gaidos, K Hofstetter, and M Alsaleh. Semi-lagrangian reproducing kernel formulation and application to modeling earth moving operations. *Mechanics of Materials*, 41(6):670–683, 2009.

[31] PC Guan, SW Chi, JS Chen, TR Slawson, and MJ Roth. Semi-lagrangian reproducing kernel particle method for fragment-impact problems. *International Journal of Impact Engineering*, 38(12):1033–1047, 2011.

[32] M Holl, S Loehnert, and P Wriggers. An adaptive multiscale method for crack propagation and crack coalescence. *International Journal for Numerical Methods in Engineering*, 93(1):23–51, 2013.

[33] Michael J Hunsweck, Yongxing Shen, and Adrián J Lew. A finite element approach to the simulation of hydraulic fractures with lag. *International Journal for Numerical and Analytical Methods in Geomechanics*, 37(9):993–1015, 2013.

[34] B. Kilic, A. Agwai, and E. Madenci. Peridynamic theory for progressive damage prediction in center-cracked composite laminates. *Composite Structures*, 90(2):141–151, 2009.

[35] Bahattin Kilic and Erdogan Madenci. Prediction of crack paths in a quenched glass plate by using peridynamic theory. *International journal of fracture*, 156(2):165–177, 2009.

[36] E. Kröner. Elasticity theory of materials with long range cohesive forces. *International Journal of Solids and Structures*, 3(5):731–742, 1967.

[37] Shaofan Li, Wei Hao, and Wing Kam Liu. Numerical simulations of large deformation of thin shell structures using meshfree methods. *Computational Mechanics*, 25(2-3):102–116, 2000.

[38] Weizhou Li and Thomas Siegmund. An analysis of crack growth in thin-sheet metal via a cohesive zone model. *Engineering Fracture Mechanics*, 69(18):2073–2093, 2002.

[39] David John Littlewood. Simulation of dynamic fracture using peridynamics, finite element modeling, and contact. Technical report, Sandia National Laboratories, 2010.

[40] Wing Kam Liu, Sukky Jun, and Yi Fei Zhang. Reproducing kernel particle methods. *International journal for numerical methods in fluids*, 20(8-9):1081–1106, 1995.

[41] Éamonn Ó Máirtín, Guillaume Parry, Glenn E Beltz, and J Patrick McGarry. Potential-based and non-potential-based cohesive zone formulations under mixed-mode separation and over-closure–part ii: Finite element applications. *Journal of the Mechanics and Physics of Solids*, 63:363–385, 2014.

[42] Bertrand Maurel and Alain Combescure. An sph shell formulation for plasticity and fracture analysis in explicit dynamics. *International journal for numerical methods in engineering*, 76(7):949–971, 2008.

[43] J Patrick McGarry, Éamonn Ó Máirtín, Guillaume Parry, and Glenn E Beltz. Potential-based and non-potential-based cohesive zone formulations under mixed-mode separation and over-closure. part i: Theoretical analysis. *Journal of the Mechanics and Physics of Solids*, 63:336–362, 2014.

[44] Jens Markus Melenk and Ivo Babuska. The partition of unity finite element method: basic theory and applications. *Computer methods in applied mechanics and engineering*, 139(1):289–314, 1996.

[45] M Memar Ardestani, B Soltani, and Sh Shams. Analysis of functionally graded stiffened plates based on fsdt utilizing reproducing kernel particle method. *Composite Structures*, 112:231–240, 2014.

[46] Y. Mikata. Analytical solutions of peristatic and peridynamic problems for a 1d infinite rod. *International Journal of Solids and Structures*, 2012.

[47] J.A. Mitchell. A nonlocal, ordinary, state-based plasticity model for peridynamics. Technical report, Sandia National Laboratories, 2011.

[48] John A Mitchell. A non-local, ordinary-state-based viscoelasticity model for peridynamics. Technical report, Tech. Report SAND2011-8064, Sandia National Laboratories, 2011.

[49] Nicolas Moes, John Dolbow, and T Belytschko. A finite element method for crack growth without remeshing. *Int. J. Numer. Meth. Engng*, 46:131–150, 1999.

[50] T Mohammadnejad and AR Khoei. Hydro-mechanical modeling of cohesive crack propagation in multiphase porous media using the extended finite element method. *International Journal for Numerical and Analytical Methods in Geomechanics*, 37(10):1247–1279, 2013.

[51] Joe J Monaghan. Smoothed particle hydrodynamics. *Reports on progress in physics*, 68(8):1703, 2005.

[52] John A Nairn. Material point method calculations with explicit cracks. *Computer Modeling in Engineering and Sciences*, 4(6):649–664, 2003.

[53] A Needleman. A continuum model for void nucleation by inclusion debonding. *Journal of applied mechanics*, 54(3):525–531, 1987.

[54] James O'Grady and John T Foster. Peridynamic beams: A non-ordinary, state-based model. *International Journal of Solids and Structures*, 51(18):3177–3183, September 2014.

[55] Michael Ortiz, Yves Leroy, and Alan Needleman. A finite element method for localized failure analysis. *Computer Methods in Applied Mechanics and Engineering*, 61(2):189–214, 1987.

[56] Mario Di Paola, Giuseppe Failla, and Massimiliano Zingales. Mechanically based nonlocal euler-bernoulli beam model. *Journal of Nanomechanics and Micromechanics*, 4(1), 2014.

[57] SC Pradhan and T Murmu. Small scale effect on the buckling of single-layered graphene sheets under biaxial compression via nonlocal continuum mechanics. *Computational Materials Science*, 47(1):268–274, 2009.

[58] Junuthula Narasimha Reddy. *Theory and analysis of elastic plates and shells*. CRC press, 2007.

[59] A. Sadeghirad, R. M. Brannon, and J. Burghardt. A convected particle domain interpolation technique to extend applicability of the material point method for problems involving massive deformations. *International Journal for Numerical Methods in Engineering*, 86(12):1435–1456, 2011.

[60] Henning Sauerland and Thomas-Peter Fries. The stable xfem for two-phase flows. *Computers & Fluids*, 87:41–49, 2013.

[61] A Shyam and E Lara-Curzio. The double-torsion testing technique for determination of fracture toughness and slow crack growth behavior of materials: a review. *Journal of materials science*, 41(13):4093–4104, 2006.

[62] S.A. Silling. Reformulation of elasticity theory for discontinuities and long-range forces. *Journal of the Mechanics and Physics of Solids*, 48(1):175–209, 2000.

[63] S.A. Silling. A coarsening method for linear peridynamics. *International Journal for Multiscale Computational Engineering*, 9(6):609, 2011.

[64] SA Silling, M. Epton, O. Weckner, J. Xu, and E. Askari. Peridynamic states and constitutive modeling. *Journal of Elasticity*, 88(2):151–184, 2007.

[65] SA Silling and RB Lehoucq. Peridynamic theory of solid mechanics. *Advances in Applied Mechanics*, 44:73–168, 2010.

[66] Stewart A Silling and Ebrahim Askari. A meshfree method based on the peridynamic model of solid mechanics. *Computers & Structures*, 83(17):1526–1535, 2005.

[67] STEWART A Silling, M Zimmermann, and R Abeyaratne. Deformation of a peridynamic bar. *Journal of Elasticity*, 73(1-3):173–190, 2003.

[68] Stewart Andrew Silling and Florin Bobaru. Peridynamic modeling of membranes and fibers. *International Journal of Non-Linear Mechanics*, 40(2):395–409, 2005.

[69] Volker Springel. Smoothed particle hydrodynamics in astrophysics. *Annual Review of Astronomy and Astrophysics*, 48:391–430, 2010.

[70] Deborah Sulsky and Howard L Schreyer. Axisymmetric form of the material point method with applications to upsetting and taylor impact problems. *Computer Methods in Applied Mechanics and Engineering*, 139(1):409–429, 1996.

[71] Michael Taylor and David J Steigmann. A two-dimensional peridynamic model for thin plates. *Mathematics and Mechanics of Solids*, 2013.

[72] Stephen Timoshenko, Sergius Woinowsky-Krieger, and S Woinowsky. *Theory of plates and shells*, volume 2. McGraw-hill New York, 1959.

[73] MR Tupek, JJ Rimoli, and R Radovitzky. An approach for incorporating classical continuum damage models in state-based peridynamics. *Computer Methods in Applied Mechanics and Engineering*, 2013.

[74] R Vignjevic, N Djordjevic, S Gemkow, T De Vuyst, and J Campbell. Sph as a nonlocal regularisation method: Solution for instabilities due to strain-softening. *Computer Methods in Applied Mechanics and Engineering*, 277:281–304, 2014.

[75] T.L. Warren, S.A. Silling, A. Askari, O. Weckner, M.A. Epton, and J. Xu. A non-ordinary state-based peridynamic method to model solid material deformation and fracture. *International Journal of Solids and Structures*, 46(5):1186–1195, 2009.

[76] O. Weckner and R. Abeyaratne. The effect of long-range forces on the dynamics of a bar. *Journal of the Mechanics and Physics of Solids*, 53(3):705–728, 2005.

[77] O. Weckner, G. Brunk, M.A. Epton, S.A. Silling, and E. Askari. Green's functions in nonlocal three-dimensional linear elasticity. *Proceedings of the Royal Society A: Mathematical, Physical and Engineering Science*, 465(2111):3463–3487, 2009.

[78] Z Wieckowski. The material point method in large strain engineering problems. *Computer methods in applied mechanics and engineering*, 193(39):4417–4438, 2004.

[79] Youcai Wu, Joseph M Magallanes, and John E Crawford. Fragmentation and debris evolution modeled by a point-wise coupled reproducing kernel/finite element formulation. *International Journal of Damage Mechanics*, page 1056789514520797, 2014.

[80] Yongning Xie and Gang Wang. A stabilized iterative scheme for coupled hydro-mechanical systems using reproducing kernel particle method. *International Journal for Numerical Methods in Engineering*, 2014.

[81] J. Xu, A. Askari, O. Weckner, and S. Silling. Peridynamic analysis of impact damage in composite laminates. *Journal of Aerospace Engineering*, 21:187, 2008.

[82] Jin Xu, Chi King Lee, and KH Tan. An xfem plate element for high gradient zones resulted from yield lines. *International Journal for Numerical Methods in Engineering*, 93(12):1314–1344, 2013.

VITA

This should be a one-page short vita.

There can be more paragraphs.